Nano Research 2016, 9(3): 787–799
DOI 10.1007/s12274-015-0958-9
Research Article
ISSN 1998-0124
CN 11-5974/O4

Facile synthesis of magnetic–plasmonic nanocomposites as T_1 MRI contrast enhancing and photothermal therapeutic agents

Zhongzhen Yang[1,2], Xianguang Ding[1,2], and Jiang Jiang[1] (✉)

[1] *Key Laboratory of Nano-Bio Interface, i-lab and Division of Nanobiomedicine, Suzhou Institute of Nano-Tech and Nano-Bionics, Chinese Academy of Sciences, Suzhou 215123, China*
[2] *University of Chinese Academy of Sciences, Beijing 100049, China*

Received: 21 September 2015
Revised: 18 November 2015
Accepted: 25 November 2015

KEYWORDS
plasmonics,
iron oxide,
photothermal,
T_1,
magnetic resonance imaging (MRI),
theranostics

ABSTRACT

Nanocomposites combining magnetic and plasmonic components have received widespread attention in recent years due to their potential applications in biomedical research. Herein, we describe a facile method for growing small iron oxide nanoparticles on various plasmonic core materials with different shapes and surfaces by utilizing a polypyrrole interlayer. By focusing on Au nanorod@polypyrrole@iron oxide (Au NR@PPy@Fe_xO) nanocomposites, we show that these systems exhibit a low r_2/r_1 ratio of 4.8, making them efficient T_1 positive contrast-enhancing agents for magnetic resonance imaging (MRI). Moreover, we show that the nanocomposites are excellent photothermal agents in the second near infrared region, with high photothermal conversion efficiency, reaching up to 46%. In addition, the Au NR@PPy@Fe_xO nanocomposites show very low cytotoxicity. In summary, the present results highlight the great potential of the synthetic method and the nanocomposites developed in this study for T_1 MRI and/or infrared thermal imaging-guided photothermal cancer therapeutic applications.

1 Introduction

Nanocomposites combining magnetic (e.g., iron oxide) and optically active plasmonic (e.g., Au) components have received widespread attention in recent years due to their potential applications in biomedical research, such as in magnetic field-assisted sensing and cancer therapies, as well as drug-delivery vehicles and imaging contrast-enhancing agents [1–4]. Such nanocomposites, possessing both magnetization and near-infrared (NIR) absorption properties, have the potential to substantially improve current cancer therapeutic treatments by enabling simultaneous imaging and therapy (theranostics) [5–7]. In these nanocomposites, the magnetic component can act as magnetic resonance imaging (MRI) agent for cancer diagnosis, due to its

Address correspondence to jjiang2010@sinano.ac.cn

high magnetic relaxivity and contrast-enhancing effect [8]; at the same time, the optically active component, with its surface plasmon resonance (SPR) characteristics, has been found to be of potential use in bio-labeling and photothermal therapy applications [9–13]. For best imaging and therapeutic results, the optical absorption of the nanocomposites needs to be tuned into the NIR region, where the light absorption and scattering by the tissues is at a minimum [14]. Thus, a tailored combination of magnetic and optically active plasmonic components is urgently needed to support MRI-guided photothermal nanotheranostics applications.

MRI is one of the most powerful medical diagnosis tools because it can provide highly detailed anatomical and functional information based on soft tissue contrast in a noninvasive way, also allowing real-time monitoring [15–21]. The MRI contrast-enhancing agents are generally categorized according to their effects on the longitudinal (T_1) and transverse (T_2) proton relaxations. T_1 contrast-enhancing agents provide a bright signal against a dark background in T_1-weighted MRI, whereas T_2 contrast-enhancing agents result in a negative contrast in T_2-weighted MRI. However, the intrinsic dark signal in T_2-weighted MRI can sometimes be misleading for the clinical diagnosis, because the labeled tumor areas are often confused with other hypointense areas such as those associated with bleeding, calcification, or metal deposition [16, 22]. Therefore, T_1 contrast-enhancing agents can be more desirable than T_2 ones for accurate high-resolution imaging. Paramagnetic compounds including Gd^{3+}, Mn^{2+}, and Fe^{3+} chelates with a large number of unpaired electrons can be used as T_1 contrast-enhancing agents [23–32]. It has been proven that the accessibility of water molecules to the paramagnetic centers is the critical factor for enhancing the resolution and signal-to-noise ratio of T_1-MRI. Although Gd^{3+} and Mn^{2+} complexes are widely used as T_1 contrast-enhancing agents, they have several disadvantages in clinical settings, including potential cytotoxicity and short circulating time due to rapid excretion in urine [33, 34]. In addition, they are difficult to functionalize for active targeting purposes. Therefore, more biofriendly nanoprobes with easy surface functionalization are critically needed as substitutes for Gd- and Mn-based T_1 MRI contrast-enhancing agents.

Iron oxide is more biocompatible than gadolinium- or manganese-based materials by virtue of the rich iron species present in the body. However, commonly prepared iron oxide nanoparticles are not appropriate for T_1-MRI, due to the high r_2/r_1 ratio (>20) derived from their intrinsic high magnetic moment. Therefore, various systems such as organic, inorganic, and inorganic/organic iron oxide hybrid nanoparticles have been developed as T_2 MRI contrast-enhancing agents [35–40]. Fortunately, the high r_2/r_1 issue can be solved by decreasing the physical size of the magnetic nanoparticles [41]. Recently, it has been demonstrated that iron oxide nanoparticles with ultra small sizes can be good candidates as T_1 agents with low toxicity, due to their reduced magnetic moment and the enhanced accessibility of Fe paramagnetic centers to water molecules [42–45]. However, to the best of our knowledge a general method to simultaneously integrate an optically active plasmonic component and iron oxide into a multifunctional theranostic platform for T_1 MRI imaging-guided photothermal therapy has not yet been demonstrated.

Herein, we report a facile but efficient route for constructing nanocomposites structured with an optically active plasmonic core and an iron oxide shell, in which Au nanocrystals of varying shapes or transition metal selenide semiconductors ($Cu_{2-x}Se$) act as the core, a thin conjugated polymer polypyrrole (PPy) works as the cohesive interlayer, and iron oxide forms the outer nanoshell. For example, with Au nanorods (Au NRs) as the core material, a conjugated polymer (PPy) was used to encapsulate the Au NRs and obtain Au NR@PPy by surfactant-assisted chemical oxidative polymerization. Then, a large number of iron oxide nanocrystals were formed on the surface of the Au NR@PPy nanoparticles, in the presence of Fe^{2+} and Fe^{3+} under alkaline conditions. The resulting Au NR@PPy@Fe_xO nanocomposites exhibit excellent NIR photothermal conversion efficiency (46%) and biocompatibility, making them promising theranostic agents for simultaneous T_1 MRI imaging and photothermal therapy.

2 Experimental

2.1 Materials

Cetyltrimethylammonium bromide (CTAB, 99%), polyvinyl alcohol (PVA, 98% hydrolyzed, average molecular weight 105,000), pyrrole (99%), and iron (III) chloride hexahydrate ($FeCl_3 \cdot 6H_2O$, 99%) were obtained from Aladdin (Shanghai, China). L-ascorbic acid, dodecyl sodium sulfate (SDS, 99%), ammonium hydroxide (NH_4OH, 28.0%–30.0%), sodium borohydride ($NaBH_4$, 96%), chloroauric acid tetrahydrate ($HAuCl_4 \cdot 4H_2O$), silver nitrate ($AgNO_3$), ferrous sulfate ($FeSO_4 \cdot 7H_2O$, 99%), hydrochloric acid (HCl, 37%), sodium oleate (NaOL, 99%), and dimethylsulfoxide (DMSO, 99%) were purchased from Sinopharm Chemical Reagent Co., Ltd. (Shanghai, China). Deionized (DI) water was used in all experiments. All chemicals were used as received without further purification.

2.2 Preparation of gold nanorods

Au NRs were synthesized by a previously described seed-mediated method [46], with some minor modifications. In a typical synthesis, CTAB-modified gold seeds were first synthesized by chemical reduction of $HAuCl_4$ with $NaBH_4$, and 250 μL of 10 mM $HAuCl_4$ was added to 9.75 mL of freshly prepared 0.1 M CTAB solution. Then, 0.6 mL of fresh ice-cold 0.01 M $NaBH_4$ was injected into the Au (III)-CTAB solution under vigorous stirring (1,200 rpm). The solution color changed from yellow to brownish yellow and the stirring was stopped after 2 min. This seed solution was aged at room temperature for 1 h before use. To prepare the growth solution, 0.7 g of CTAB and 0.1234 g of NaOL were dissolved in 25 mL of warm water (~50 ℃). The solution was allowed to cool down to 30 ℃ and 480 μL of 0.02 M $AgNO_3$ solution was added. The mixture was kept undisturbed at 30 ℃ for 15 min, after which 25 mL of 1 mM $HAuCl_4$ solution was added. The solution became colorless after 90 min of stirring (700 rpm), and 300 μL of HCl (37 wt.% in water, 12.1 M) was then introduced to adjust the solution pH. After another 15 min of slow stirring at 400 rpm, 80 μL of 0.1 M ascorbic acid (AA) was added and the solution was vigorously stirred for 30 s. Finally, 40 μL of as-synthesized seeds solution was injected into the growth medium. The resultant mixture was stirred for 30 s and left undisturbed at 30 ℃ for 12 h for NR growth. The final products were isolated by centrifugation at 9,000 rpm for 20 min, followed by removal of the supernatant. After discarding the supernatant, the precipitate was dispersed in 20 mL of DI water for the next step, i.e., the synthesis of polypyrrole-coated Au NRs hybrid nanomaterials.

2.3 Preparation of Au NR@PPy nanocomposites

As soon as the Au NRs were synthesized, 5 mL of aqueous solution of Au NRs, 300 μL of 40 mM SDS aqueous solution, and 200 μL of pyrrole monomer were mixed together under vigorous stirring. Subsequently, 3 mL of 2 mM acidic $(NH_4)_2S_2O_8$ solution was added. After being stirred for 10 s, the reaction mixture was incubated at room temperature for 2 h to complete the oxidative polymerization, until the color of mixture turned to black. The PPy-coated NRs were purified by centrifugation at 9,000 rpm for 10 min, repeated three times. After removal of the supernatant, the concentrated PPy-coated Au NRs solution was collected at the bottom of the centrifuge tube.

2.4 Preparation of Au NR@PPy@Fe_xO nanocomposites

The Au NR@PPy nanocomposites solution obtained in the above step was diluted with 2 mL DI water and 3 mL PVA (1%) aqueous solution under N_2 atmosphere with vigorous stirring for 0.5 h. Then, 15 μL of a mixture of 0.214 M $FeCl_3$ and 0.107 M $FeCl_2$ solutions was added under N_2 atmosphere with vigorous stirring. After 0.5 h, 300 μL of NH_4OH (9%) solution was quickly injected into the reaction solution at 70 ℃ under N_2 atmosphere for another 1 h. The final products were purified by centrifuging twice at 9,500 rpm for 10 min. The supernatant was discarded and the precipitate was redispersed in water under ambient conditions.

2.5 Synthesis of other plasmonic core nanomaterials

Au nanoparticles (d ~ 17 nm) [47], Au nanostars (d ~ 40 nm) [48], Au triangular nanoplates (d ~ 65 nm) [49], and $Cu_{2-x}Se$ nanoparticles (d ~ 30 nm) [50] were prepared separately following published procedures.

2.6 Synthesis of core@PPy@Fe$_x$O core–shell nanocomposites with different cores

Five mL of the aqueous solution of Au nanoparticles, Au nanostars, Au triangular nanoplates, or $Cu_{2-x}Se$ nanoparticles were mixed with 300 μL aqueous solution of 40 mM SDS and 200 μL of pyrrole monomer under vigorous stirring. Subsequently, 3 mL of 2 mM acidic $(NH_4)_2S_2O_8$ solution was added. After being stirred for 10 s, the reaction mixture was incubated at room temperature for 2 h to complete the oxidative polymerization process. Then, these PPy-coated nanostructures were purified by centrifugation at 9,000 rpm for 10 min, repeated three times. After removing the supernatant, the concentrated PPy-coated nanocomposites solutions were used to grow iron oxide nanoshells in the same way as described in section 2.4 above.

2.7 Characterization

The morphology and size of the synthesized nanocomposites were characterized by transmission electron microscopy (TEM) and scanning transmission electron microscopy (STEM), using a FEI Technai G2 S-Twin instrument at an acceleration voltage of 200 kV. The sizes of all as-prepared nanomaterials were determined from TEM micrographs using the ImageJ software (V1.41, NIH, USA) for image analysis. The elemental composition was analyzed by an energy-dispersive X-ray spectroscopy (EDX) analyzer as TEM accessory. UV–vis–NIR spectra were recorded on a Lambda-25 spectrophotometer (PerkinElmer Inc., USA) under ambient conditions. Au and Fe concentrations of the nanocomposite solution were measured by an inductively coupled plasma optical emission spectrometer (ICP-OES, PerkinElmer 2100 DV). The MRI relaxation properties of the Au NR@PPy@Fe$_x$O nanocomposites (0.054–0.216 mM Fe) were scanned with a 0.5 T NMR analyzer (Shanghai Huantong Corporation, GY-PNMR-10). The measurement parameters were set as follows: repetition time (TR) = 500 ms; echo time (TE) = 30 ms; number of excitations (NEX) = 1. The relaxation rates r_1 and r_2 were calculated by a linear fit of the $1/T_1$ and $1/T_2$ relaxation times versus the Fe concentration (mM). The tetrazolium colorimetric assay (MTT) was conducted using a Biotek Elx 800 Microplate Reader.

2.8 Photothermal performance of Au NR@PPy@Fe$_x$O nanocomposites in aqueous solution

To evaluate the photothermal heating performances of the as-synthesized Au NR@PPy@Fe$_x$O nanocomposites, 1.5 mL of an aqueous dispersion of Au NR@PPy@Fe$_x$O of different concentrations was placed in a quartz cuvette and exposed to a 1,064 nm laser at different power densities for 5 min. A thermocouple probe with an accuracy of 0.1 ˚C was inserted into the nanocomposites solutions perpendicular to the laser path to avoid direct light irradiation on the probe. The temperature was recorded every 20 s by a digital thermometer.

2.9 Cytotoxicity assay of Au NR@PPy@Fe$_x$O nanocomposites

The cytotoxicity of the nanocomposites was evaluated on neural stem cells (NSC) by MTT assay. Briefly, the NSC cells were seeded into 96-well plates at a density of 1×10^4 cells per well and cultured for 24 h to allow cells to attach at 37 ˚C in a humidified incubator, in which the CO_2 level was maintained constant at 5%. Afterward, the original culture medium was changed to fresh medium, or to Au NR@PPy@Fe$_x$O dispersions in medium at the desired concentrations (50, 100, 150, and 200 μM Au, respectively) for 24 h at 37 ˚C. Subsequently, the medium was removed and replaced by 10 μL of MTT reagent in 100 μL of serum-free medium. After being incubated for additional 4 h at 37 ˚C, the absorbance of each well at 490 nm was measured using a microplate reader. The relative cell viability was calculated as $100\% \times A_{test}/A_{control}$ (where A_{test} and $A_{control}$ are the absorbance of a well treated with and without Au NR@PPy@Fe$_x$O nanocomposites, respectively), with three replicates carried out for each treatment group.

3 Results and discussion

3.1 Synthesis of Au NR@PPy@Fe$_x$O nanocomposites

The strategy to synthesize Au NR@PPy@Fe$_x$O nanocomposites involved surfactant-assisted chemical oxidative polymerization of pyrrole on the surface of Au NRs, and subsequent formation of iron oxide

nanocrystals at the outer shell of the Au NR@PPy nanocomposite in the presence of Fe^{2+} and Fe^{3+} under alkaline conditions, as illustrated in Scheme 1. In particular, anionic surfactant SDS was first absorbed onto the CTAB layers on Au NRs through electrostatic interactions. Then, the pyrrole monomers introduced into the aqueous solution were trapped within the surfactant layers. Following the addition of an oxidant (ammonium persulfate, $(NH_4)_2S_2O_8$), pyrrole polymerization occurred, resulting in the coating of a PPy shell onto the surface of the Au NRs. In this polymerization process, surfactant SDS served as a stabilizing agent, preventing Au NRs aggregation and allowing single NR encapsulation upon polymerization [51–53].

In order to form iron oxide on Au NR@PPy, an aqueous solution containing Fe^{3+}, PVA, and Fe^{2+} was added into the system under N_2 protection. The formed Au NR@PPy nanocomposites can be modified by PVA, which functions as a capping agent to make the particles highly hydrophilic [54–56]. Then, an ammonia solution was dropped into the system with moderate heating at 70 ˚C to coprecipitate the Fe^{3+} and Fe^{2+} ions, forming small iron oxide nanocrystals on the Au NR@PPy nanocomposites.

Another way to coat PPy on Au NRs is by Fe^{3+}-mediated oxidative polymerization [56–59]. Compared to the method using ammonium persulfate oxidant, the polymerization process with Fe^{3+} as oxidant was much faster and therefore difficult to control. Moreover, we found that the surfactant SDS influences the formation of Au NR@PPy nanoparticles prepared by Fe^{3+}-mediated oxidative polymerization, since the excess surfactant SDS can act as a soft template for free PPy formation. By increasing the added amount of SDS, the amount of free PPy in solution increased, along with a clear damping of the SPR absorption from Au NRs (Fig. S1 in the Electronic Supplementary Material (ESM)). Furthermore, a large amount of ferric and ferrous ions from the starting Fe^{3+} and its reduced form remained in the obtained Au NR@PPy solution. When the ammonia solution was added directly into the above Au NR@PPy solution without centrifugation, iron oxide nanoparticles could form *in situ* both on the Au NR@PPy nanocomposites and in solution (Fig. S2 in the ESM), likely due to the large amount of free PPy formed in the reaction solution. One concern with the Fe^{3+}-mediated polymerization is the oxidative etching exerted by Fe^{3+} on the Au NRs. In order to check whether the strong damping observed in Fig. S1(d) (in the ESM) is due to this effect, the optical extinction spectra of the prepared Au NRs before and after Fe^{3+} treatment have been measured and compared (Fig. S3 in the ESM). The results highlight a slight decrease in intensity and a blue shift of the longitudinal SPR peak, indicating chemical etching of Fe^{3+} on Au NRs. However, based on the magnitude of this change, the involvement of Fe^{3+} in the large damping of the Au NRs SPR can be ruled out.

The excess PPy in solution can be removed by centrifuging the Au NR@PPy dispersion. A colorimetric determination of the iron species showed that only a small amount of ferric ions and no ferrous ions were left after centrifugation (Fig. S4 in the ESM). Therefore,

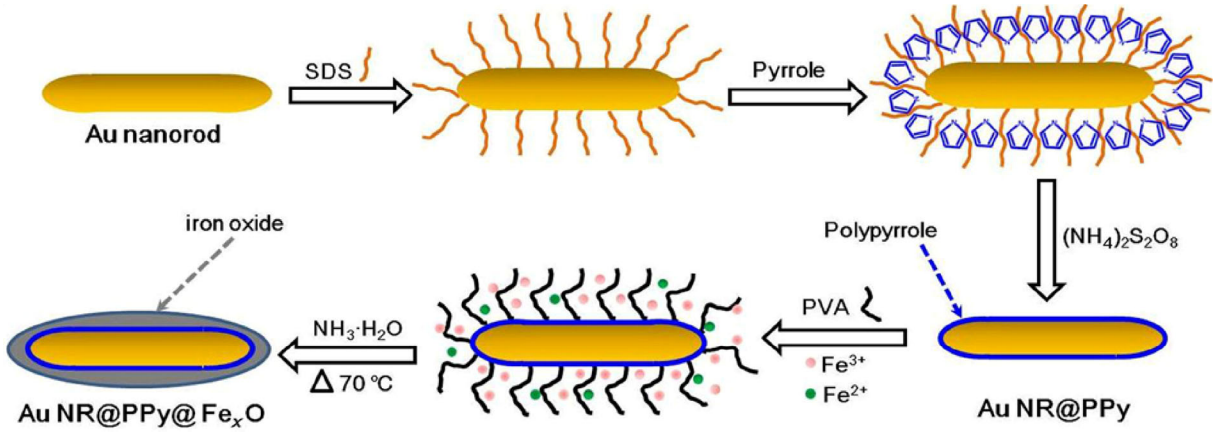

Scheme 1 Schematic diagram illustrating the synthesis of Au NR@PPy@Fe_xO nanocomposites.

by adding a small amount of Fe^{2+} under alkaline conditions, iron oxide nanocrystals can form on the outer shell of the Au NR@PPy nanocomposites (Fig. S5 in the ESM), suppressing free iron oxides formation in solution. However, due to fast polymerization when Fe^{3+} was used as oxidant, neat PPy-encapsulated Au NRs cannot be obtained (only thicker and irregular PPy).

We also investigated the effect of the concentration of ferric and ferrous ions on the formation of the nanocomposites. With the concentration of ferric and ferrous ions increased, the TEM image contrast of the shell in the nanocomposites became darker, due to larger amount of deposited iron oxides. When the concentration of ferric and ferrous ions was high enough, free iron oxides became clearly evident in the reaction mixture (Fig. S6 in the ESM). Therefore, the concentration of ferric and ferrous ions should be kept below an optimal concentration in order to avoid the formation of free iron oxide nanocrystals.

Previous work demonstrated that PPy, a conducting polymer, can support the adhesion and growth of different cell types and does not irritate the immune system of mammalians, due to its high conductivity and good biocompatibility [59–61]. In this study, the thin PPy shell has served as cohesive layer to facilitate coating of small iron oxides on the Au NRs. In the absence of the PPy layer, iron oxides can still grow

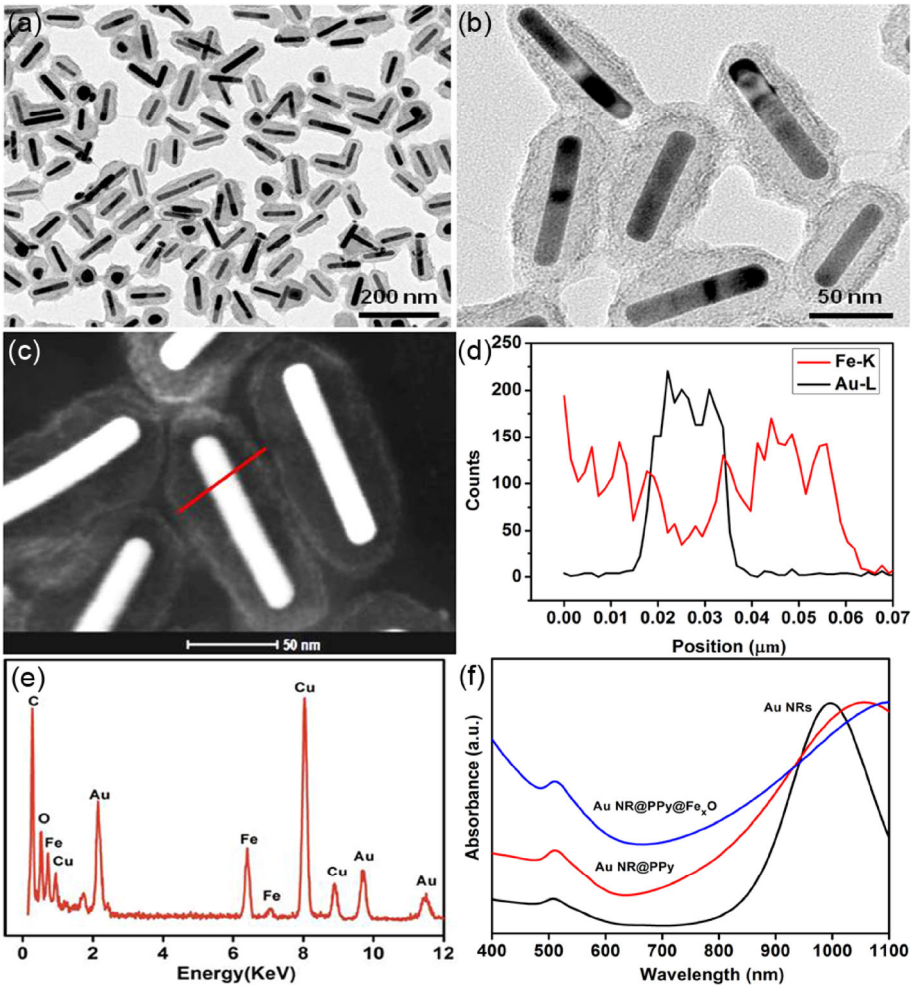

Figure 1 (a) and (b) TEM images at different magnifications of the as-synthesized Au NR@PPy@Fe_xO nanocomposites. (c) STEM image of the Au NR@PPy@Fe_xO nanocomposites. (d) EDX elemental line scanning profiles for Au and Fe, showing that Fe is present in the nanocomposites, distributed along the outer rim of the polymer shell. (e) Bulk EDX analysis of Au NR@PPy@Fe_xO nanocomposites showing the presence of Au and Fe (Cu from the TEM grid). (f) UV–vis–NIR absorption spectra of the Au NRs, Au NR@PPy, and Au NR@PPy@Fe_xO nanocomposites.

along the outer border of the Au NRs, albeit in a very uneven manner (Fig. S7 in the ESM).

3.2 Characterization of Au NR@PPy@Fe$_x$O nanocomposites

As discussed above, under optimized experimental conditions, uniform Au NR@PPy@Fe$_x$O nanocomposites exhibiting an evident core–shell structure were successfully synthesized, as shown in Figs. 1(a) and 1(b). The size of the Au NR core is 16 nm × 92 nm, whereas that of the PPy coating is ~18 nm, and the iron oxide nanoparticles display a very small size (difficult to identify by TEM). The STEM image clearly shows that Fe$_x$O nanoparticles (NPs) are distributed along the outer rim of the polymer shell, judging from the image contrast (Fig. 1(c)) as well as the elemental line profiles (Fig. 1(d)). The elemental composition of the as-synthesized nanocomposites over a larger area was determined using EDX (Fig. 1(e)), further confirming the presence of Fe. The X-ray diffraction (XRD) patterns of the nanocomposites only display Au diffraction peaks (Fig. S8 in the ESM), indicating either very small or amorphous iron oxide nanoparticles.

Next, UV–vis–NIR spectroscopy measurements were conducted to analyze the surface plasmon resonance features of the Au NRs, Au NR@PPy, and Au NR@PPy@Fe$_x$O nanocomposites. As shown in Fig. 1(f), the localized surface plasmon resonance (LSPR) of Au NRs was centered at ~980 nm. This peak was red-shifted by 100 nm after PPy shell coating as a result of the changed dielectric environment. The Au NR@PPy@Fe$_x$O exhibited a broader and further damped LSPR peak extending from the visible to the NIR region with a maximum at nearly 1,100 nm.

3.3 Magnetic resonance relaxivity measurement

The relaxivity of the as-synthesized Au NR@PPy@Fe$_x$O nanocomposites was examined to evaluate their potential use as MR contrast-enhancing agents.

Figures 2(a) and 2(b) show the longitudinal ($1/T_1$) and transverse ($1/T_2$) relaxation rates of protons in Au NR@PPy@Fe$_x$O aqueous solution as a function of the iron concentration at 0.5 T magnetic field. The longitudinal relaxivity (r_1, i.e., the longitudinal relaxation rate per mM of iron) and transverse relaxivity (r_2, transverse relaxation rate per mM of iron) of the Au NR@PPy@Fe$_x$O were estimated to be 1.07 and 5.1 mM^{-1}·S^{-1}, respectively. The r_2/r_1 ratio measured for the Au NR@PPy@Fe$_x$O nanocomposites is thus 4.8. The measured relaxivity of 1.07 mM^{-1}·S^{-1} is comparable to that recently reported for FeOOH-silica nanocomposites (0.48–2.12 mM^{-1}·S^{-1}) by Chou and coworkers [62]. Their relatively low r_2/r_1 value demonstrates that Au NR@PPy@Fe$_x$O has the potential to be utilized as an effective T_1-weighted positive contrast-enhancing agent for MRI. We also investigated the MR relaxivity of the Au NR@PPy@Fe$_x$O nanocomposites with different iron oxides densities (samples shown in Figs. S6(b) and S6(d) in the ESM). It was found that the r_1 and r_2 values do not depend on the amount of iron oxide nanocrystals in the nanocomposites (Fig. S9 in the ESM). In contrast, larger Fe$_x$O on Au NR@PPy showed a much higher r_2/r_1 value (~9), making them effective T_2-weighted negative contrast-enhancing agents for MRI, with no apparent Fe$_x$O NP density dependence observed either (Fig. S10 in the ESM).

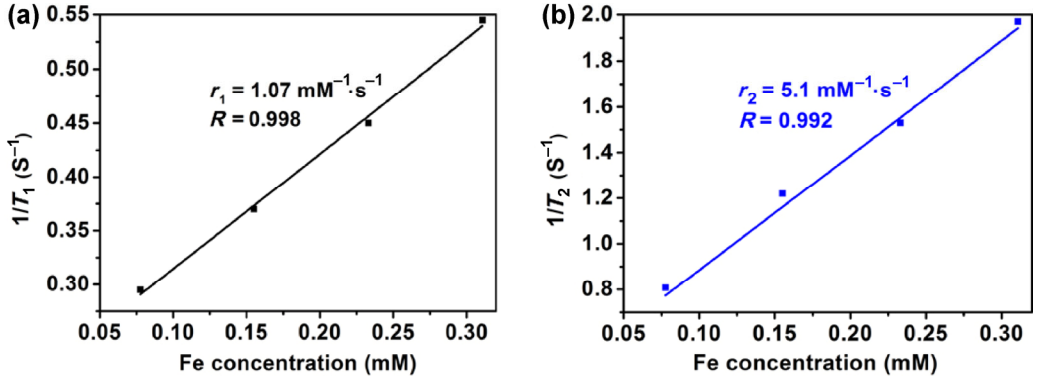

Figure 2 T_1 (a) and T_2 (b) relaxation rate of the Au NR@PPy@Fe$_x$O nanocomposites as a function of the iron concentration.

Our results are significantly different from those first reported by Han et al [58], and more recently by He and coworkers [57], on the formation of iron oxide nanocrystals on PPy NPs or shells. The iron oxide synthesized here has a much smaller size, making it better suited for enhancing the T_1 MRI contrast [42–45]. The small nanocrystal size is a result of the experimental protocol employed here, in particular, the use of a thin PPy layer prepared by ammonium persulfate oxidative polymerization and the addition of PVA.

3.4 Photothermal performance of Au NR/PPy@Fe_xO nanocomposites

Photothermal therapy is an emerging technique that utilizes photothermal agents to convert photons into local heat and kill cancer cells at the target tumor sites. The photothermal properties of the Au NR@PPy@Fe_xO nanocomposites were first studied by monitoring the temperature change of 1.5 mL of Au NR@PPy@Fe_xO nanocomposites solution at various concentrations (spanning 50–200 μM Au) under the irradiation of a 1,064 nm continuous wave laser. At a laser power density of 1 W/cm^2, with the nanocomposites concentration increasing, the solution temperature elevation increased from 10 to 16.5 ℃ after 5 min of laser irradiation, while pure water showed little heating effect at the same power density (Fig. 3(a)). The final temperature increase at the end of the laser irradiation period as a function of the nanocomposites concentration is plotted in Fig. 3(b). The temperature elevation profile flattens out with increasing nanocomposites concentrations, due to the logarithmic absorbance dependence on the fraction of incident radiation. When the nanocomposites concentration was fixed at 200 μM, a strong dependence of the photothermal effect of the nanocomposites on the laser power clearly emerged, with the highest temperature elevation up to 16.5 ℃ obtained at 1 W/cm^2 (Fig. 3(c)). These results indicate that the Au NR@PPy@Fe_xO nanocomposites can rapidly and efficiently convert the energy of a 1,064 nm laser into thermal energy.

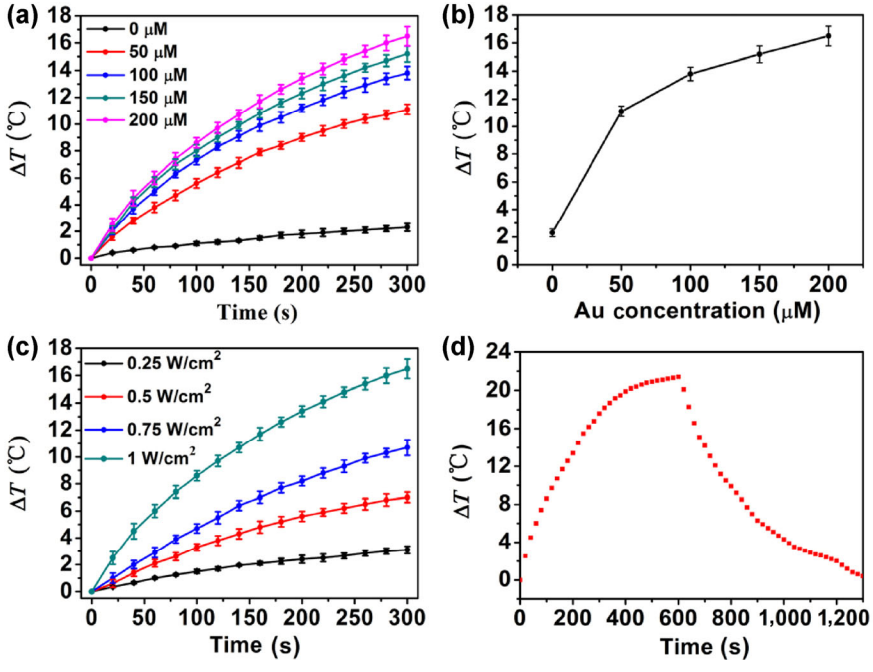

Figure 3 (a) Temperature elevation curves of plain water (0 μM) and Au NR@PPy@Fe_xO nanocomposites aqueous solutions at different concentrations (50–200 μM) under laser irradiation. (b) Temperature change versus concentration of Au NR@PPy@Fe_xO nanocomposites after exposure to laser for 5 min. (c) Temperature elevation profiles of 200 μM Au NR@PPy@Fe_xO nanocomposites aqueous solutions under different laser power densities. (d) Monitored temperature profile of Au NR@PPy@Fe_xO nanocomposites aqueous solution (200 μM) irradiated by laser for 600 s, followed by natural cooling with laser light turned off. Unless otherwise noted, a 1,064 nm laser was used at a power density of 1 W/cm^2, and the error bars represent standard deviations (n = 3).

In all present photothermal measurements, the nanocomposites solution was exposed to laser for three times and a similar temperature change was observed, indicating good photostability of the Au NR@PPy@Fe_xO nanocomposites.

To further quantify the photothermal transduction efficiency, we recorded the temperature change of the 200 μM solution as a function of time, under continuous irradiation by a 1,064 nm laser for 600 s at the power density of 1 W/cm^2 (Fig. 3(d)). The nanocomposite dispersions were illuminated until reaching a steady state temperature, at which point the light source was removed, and the solution was allowed to cool down naturally. During this cooling stage, the temperature decrease was monitored to determine the rate of heat dissipation from the system to the environment, which was obtained by fitting the measured cooling curve (Fig. S11 in the ESM). According to the obtained data and the reported method [63, 64], the photothermal conversion efficiency of the Au NR@PPy@Fe_xO nanocomposites can reach up to 46%. As Au NRs are reported to have a lower photothermal transduction efficiency of ~25%, experiments on Au NR and Au NR@PPy were also conducted. These systems were found to exhibit lower conversion efficiency of 28.6% (Fig. S12 in the ESM) and 37.5% (Fig. S13 in the ESM), respectively. Furthermore, the photothermal performance of a black Fe_xO colloidal solution was also checked, and the measured conversion efficiency was 36.5% (Fig. S14 in the ESM). These results clearly show that the Au NR@PPy@Fe_xO nanocomposites are highly efficient and photostable photothermal agents.

3.5 Cytotoxicity of Au NR@PPy@Fe_xO nanocomposites

Au, PPy, and iron oxide are all known to be biocompatible with little cytotoxicity. The cytotoxicity of the synthesized Au NR@PPy@Fe_xO nanocomposites was evaluated on neural stem cells using the standard MTT assay (Fig. S15 in the ESM). NSC cells incubated with Au NR@PPy@Fe_xO nanocomposites did not display any obvious cytotoxicity over a wide concentration range (0–200 μM Au) for 24 h. The percentages of viable cells for NSC were 82.0% ± 8.4%, after being exposed to the nanocomposites with a concentration of 200 μM Au for 24 h, demonstrating good biocompatibility of the Au NR@PPy@Fe_xO nanocomposites, and confirming their great potential to be used as biocompatible theranostic agents.

3.6 General method for coating iron oxides on different cores

PPy coating and subsequent growth of an iron oxide shell on nanocrystals is a facile and cost-effective method, which is also independent of the geometry and composition of the core materials and surface properties. Using the thin polymeric PPy shell as cohesive layer, we extended the coating of iron oxides onto a variety of different materials. For example, we have successfully fabricated Au triangular-plate@PPy@Fe_xO (Figs. 4(a) and 4(e)), Au nanostar@PPy@Fe_xO (Figs. 4(b) and 4(f)), and Au nanoparticle@PPy@Fe_xO (Figs. 4(c) and 4(g)) nanocomposites by using various Au core shapes. In addition, semiconductor $Cu_{2-x}Se$ was also prepared to

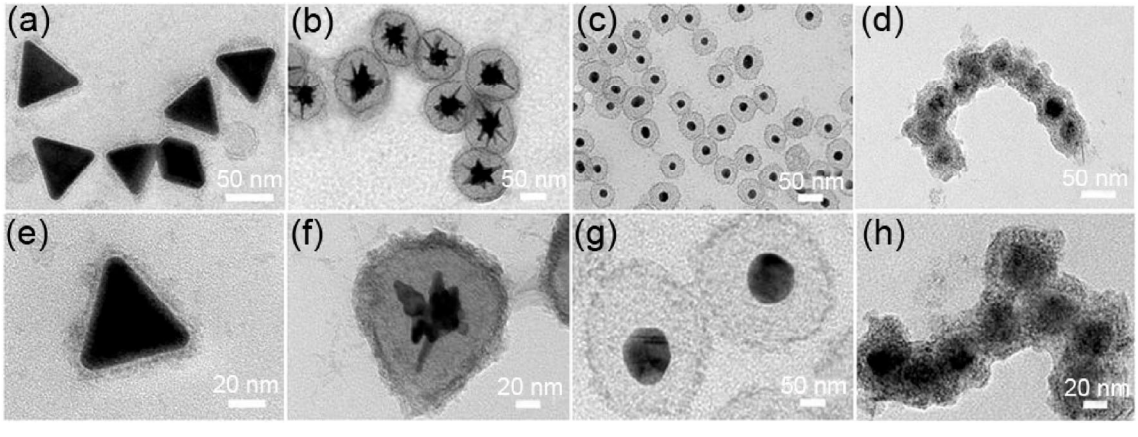

Figure 4 TEM images of core@PPy@Fe_xO nanocomposites with different core materials: (a) and (e) Au triangular nanoplates; (b) and (f) Au nanostars; (c) and (g) Au nanoparticles; (d) and (h) $Cu_{2-x}Se$ nanoparticles.

form $Cu_{2-x}Se$@PPy@Fe_xO nanocomposites (Figs. 4(d) and 4(h)).

These as-synthesized nanocomposites, with both an optically active plasmonic core and a magnetic shell, have the potential to be used in future applications as both magnetic resonance imaging and photothermal therapy agents for simultaneously performing imaging and therapeutic administrations.

4 Conclusions

In summary, we have developed a facile and versatile strategy that enables formation of small iron oxide nanocrystals on a variety of cores made of different materials with the help of a thin inner-layer PPy as cohesive layer. The obtained Au NR@PPy@Fe_xO nanocomposites were found to be effective photothermal agents, exhibiting good dispersity, intense NIR absorption, photostability, and high photothermal conversion efficiency. Additionally, we demonstrated that these nanocomposites can be used as effective contrast agent for T_1 MRI imaging. Furthermore, the nanocomposites show very low cytotoxicity, which highlights their potential use as biocompatible multifunctional photothermal agents. Therefore, we anticipate that the nanocomposites developed in this study have great potential for T_1-MRI and/or infrared thermal imaging-guided photothermal cancer therapeutic applications.

Acknowledgements

This work is funded by the "Hundred Talents" program of Chinese Academy of Sciences, and National Natural Science Foundation of China (Nos. 21175148 and 21473243).

Electronic Supplementary Material: Supplementary material (Au NR@PPy@Fe_xO prepared under different conditions, Fe^{3+} etching effect on Au NR, XRD patterns, relaxivity measurements, NP cytotoxicity, results for photothermal transduction efficiencies of Au NR, Au NR@PPy and Fe_xO) is available in the online version of this article at http://dx.doi.org/10.1007/s12274-015-0958-9.

References

[1] Dong, W. J.; Li, Y. S.; Niu, D. C.; Ma, Z.; Gu, J. L.; Chen, Y.; Zhao, W. R.; Liu, X. H.; Liu, C. S.; Shi, J. L. Facile synthesis of monodisperse superparamagnetic Fe_3O_4 Core@hybrid@Au shell nanocomposite for bimodal imaging and photothermal therapy. *Adv. Mater.* **2011**, *23*, 5392–5397.

[2] Xu, C. J.; Wang, B. D.; Sun, S. H. Dumbbell-like Au-Fe_3O_4 nanoparticles for target-specific platin delivery. *J. Am. Chem. Soc.* **2009**, *131*, 4216–4217.

[3] Bardhan, R.; Chen, W. X.; Bartels, M.; Perez-Torres, C.; Botero, M. F.; McAninch, R. W.; Contreras, A.; Schiff, R.; Pautler, R. G.; Halas, N. J. et al. Tracking of multimodal therapeutic nanocomplexes targeting breast cancer *in vivo*. *Nano Lett.* **2010**, *10*, 4920–4928.

[4] Lal, S.; Clare, S. E.; Halas, N. J. Nanoshell-enabled photothermal cancer therapy: Impending clinical impact. *Acc. Chem. Res.* **2008**, *41*, 1842–1851.

[5] Wang, C. G.; Chen, J. J.; Talavage, T.; Irudayaraj, J. Gold nanorod/Fe_3O_4 nanoparticle "nano-pearl-necklaces" for simultaneous targeting, dual-mode imaging, and photothermal ablation of cancer cells. *Angew. Chem., Int. Ed.* **2009**, *48*, 2759–2763.

[6] Liong, M.; Lu, J.; Kovochich, M.; Xia, T.; Ruehm, S. G.; Nel, A. E.; Tamanoi, F.; Zink, J. I. Multifunctional inorganic nanoparticles for imaging, targeting, and drug delivery. *ACS Nano* **2008**, *2*, 889–896.

[7] Larson, T. A.; Bankson, J.; Aaron, J.; Sokolov, K. Hybrid plasmonic magnetic nanoparticles as molecular specific agents for MRI/optical imaging and photothermal therapy of cancer cells. *Nanotechnology* **2007**, *18*, 325101.

[8] Ma, L. L.; Feldman, M. D.; Tam, J. M.; Paranjape, A. S.; Cheruku, K. K.; Larson, T. A.; Tam, J. O.; Ingram, D. R.; Paramita, V.; Villard, J. W. et al. Small multifunctional nanoclusters (nanoroses) for targeted cellular imaging and therapy. *ACS Nano* **2009**, *3*, 2686–2696.

[9] El-Sayed, I. H.; Huang, X. H.; El-Sayed, M. A. Surface plasmon resonance scattering and absorption of anti-EGFR antibody conjugated gold nanoparticles in cancer diagnostics: Applications in oral cancer. *Nano Lett.* **2005**, *5*, 829–834.

[10] Wu, X.; Ming, T.; Wang, X.; Wang, P. N.; Wang, J. F.; Chen, J. Y. High-photoluminescence-yield gold nanocubes: For cell imaging and photothermal therapy. *ACS Nano* **2010**, *4*, 113–120.

[11] Novo, C.; Funston, A. M.; Pastoriza-Santos, I.; Liz-Marzán, L. M.; Mulvaney, P. Spectroscopy and high-resolution microscopy of single nanocrystals by a focused ion beam registration method. *Angew. Chem., Int. Ed.* **2007**, *46*, 3517–3520.

[12] Kennedy, L. C.; Bickford, L. R.; Lewinski, N. A.; Coughlin, A. J.; Hu, Y.; Day, E. S.; West, J. L.; Drezek, R. A. A new era for cancer treatment: Gold-nanoparticle-mediated thermal therapies. *Small* **2011**, *7*, 169–183.

[13] Chen, J. Y.; Glaus, C.; Laforest, R.; Zhang, Q.; Yang, M. X.; Gidding, M.; Welch, M. J.; Xia, Y. N. Gold nanocages as photothermal transducers for cancer treatment. *Small* **2010**, *6*, 811–817.

[14] Hirsch, L. R.; Stafford, R. J.; Bankson, J. A.; Sershen, S. R.; Rivera, B.; Price, R. E.; Hazle, J. D.; Halas, N. J.; West, J. L. Nanoshell-mediated near-infrared thermal therapy of tumors under magnetic resonance guidance. *Proc. Natl. Acad. Sci. USA* **2003**, *100*, 13549–13554.

[15] Weissleder, R.; Pittet, M. J. Imaging in the era of molecular oncology. *Nature* **2008**, *452*, 580–589.

[16] Na, H. B.; Hyeon, T. Nanostructured T_1 MRI contrast agents. *J. Mater. Chem.* **2009**, *19*, 6267–6273.

[17] Na, H. B.; Song, I. C.; Hyeon, T. Inorganic nanoparticles for MRI contrast agents. *Adv. Mater.* **2009**, *21*, 2133–2148.

[18] Jun, Y. W.; Huh, Y. M.; Choi, J. S.; Lee, J. H.; Song, H. T.; Kim, S.; Yoon, S.; Kim, K. S.; Shin, J. S.; Suh, J. S. et al. Nanoscale size effect of magnetic nanocrystals and their utilization for cancer diagnosis via magnetic resonance imaging. *J. Am. Chem. Soc.* **2005**, *127*, 5732–5733.

[19] Jun, Y.-W.; Seo, J.-W.; Cheon, A. Nanoscaling laws of magnetic nanoparticles and their applicabilities in biomedical sciences. *Acc. Chem. Res.* **2008**, *41*, 179–189.

[20] Huh, Y. M.; Jun, Y. W.; Song, H. T.; Kim, S.; Choi, J. S.; Lee, J. H.; Yoon, S.; Kim, K. S.; Shin, J. S.; Suh, J. S. et al. *In vivo* magnetic resonance detection of cancer by using multifunctional magnetic nanocrystals. *J. Am. Chem. Soc.* **2005**, *127*, 12387–12391.

[21] Gao, J. H.; Liang, G. L.; Cheung, J. S.; Pan, Y.; Kuang, Y.; Zhao, F.; Zhang, B.; Zhang, X. X.; Wu, E. X.; Xu, B. Multifunctional yolk–shell nanoparticles: A potential MRI contrast and anticancer agent. *J. Am. Chem. Soc.* **2008**, *130*, 11828–11833.

[22] Lee, N.; Kim, H.; Choi, S. H.; Park, M.; Kim, D.; Kim, H.-C.; Choi, Y.; Lin, S.; Kim, B. H.; Jung, H. S. et al. Magnetosome-like ferrimagnetic iron oxide nanocubes for highly sensitive MRI of single cells and transplanted pancreatic islets. *Proc. Natl. Acad. Sci. USA* **2011**, *108*, 2662–2667.

[23] Caravan, P. Strategies for increasing the sensitivity of gadolinium based MRI contrast agents. *Chem. Soc. Rev.* **2006**, *35*, 512–523.

[24] Hifumi, H.; Yamaoka, S.; Tanimoto, A.; Citterio, D.; Suzuki, K. Gadolinium-based hybrid nanoparticles as a positive MR contrast agent. *J. Am. Chem. Soc.* **2006**, *128*, 15090–15091.

[25] Park, Y. I.; Kim, J. H.; Lee, K. T.; Jeon, K.-S.; Na, H. B.; Yu, J. H.; Kim, H. M.; Lee, N.; Choi, S. H.; Baik, S.-I. et al. Nonblinking and nonbleaching upconverting nanoparticles as an optical imaging nanoprobe and T_1 magnetic resonance imaging contrast agent. *Adv. Mater.* **2009**, *21*, 4467–4471.

[26] Bridot, J.-L.; Faure, A.-C.; Laurent, S.; Rivière, C.; Billotey, C.; Hiba, B.; Janier, M.; Josserand, V.; Coll, J.-L.; Vander Elst, L. et al. Hybrid gadolinium oxide nanoparticles: Multimodal contrast agents for *in vivo* imaging. *J. Am. Chem. Soc.* **2007**, *129*, 5076–5084.

[27] Rieter, W. J.; Kim, J. S.; Taylor, K. M. L.; An, H.; Lin, W. L.; Tarrant, T.; Lin, W. B. Hybrid silica nanoparticles for multimodal imaging. *Angew. Chem., Int. Ed.* **2007**, *46*, 3680–3682.

[28] Na, H. B.; Lee, J. H.; An, K.; Park, Y. I.; Park, M.; Lee, I. S.; Nam, D.-H.; Kim, S. T.; Kim, S.-H.; Kim, S.-W. et al. Development of a T_1 contrast agent for magnetic resonance imaging using MnO nanoparticles. *Angew. Chem., Int. Ed.* **2007**, *46*, 5397–5401.

[29] Choi, S.-H.; Na, H. B.; Park, Y. I.; An, K.; Kwon, S. G.; Jang, Y.; Park, M.-H.; Moon, J.; Son, J. S.; Song, I. C. et al. Simple and generalized synthesis of oxide-metal hetero-structured nanoparticles and their applications in multimodal biomedical probes. *J. Am. Chem. Soc.* **2008**, *130*, 15573–15580.

[30] An, K.; Kwon, S. G.; Park, M.; Na, H. B.; Baik, S.-I.; Yu, J. H.; Kim, D.; Son, J. S.; Kim, Y. W.; Song, I. C. et al. Synthesis of uniform hollow oxide nanoparticles through nanoscale acid etching. *Nano Lett.* **2008**, *8*, 4252–4258.

[31] Yang, H.; Zhuang, Y. M.; Hu, H.; Du, X. X.; Zhang, C. X.; Shi, X. Y.; Wu, H. X.; Yang, S. P. Silica-coated manganese oxide nanoparticles as a platform for targeted magnetic resonance and fluorescence imaging of cancer cells. *Adv. Funct. Mater.* **2010**, *20*, 1733–1741.

[32] Kim, T.; Momin, E.; Choi, J.; Yuan, K.; Zaidi, H.; Kim, J.; Park, M.; Lee, N.; McMahon, M. T.; Quinones-Hinojosa, A. et al. Mesoporous silica-coated hollow manganese oxide nanoparticles as positive T_1 contrast agents for labeling and MRI tracking of adipose-derived mesenchymal stem cells. *J. Am. Chem. Soc.* **2011**, *133*, 2955–2961.

[33] Penfield, J. G.; Reilly, R. F., Jr. What nephrologists need to know about gadolinium. *Nat. Clin. Pract. Nephrol.* **2007**, *3*, 654–668.

[34] Limbach, L. K.; Wick, P.; Manser, P.; Grass, R. N.; Bruinink, A.; Stark, W. J. Exposure of engineered nanoparticles to human lung epithelial cells: Influence of chemical composition and catalytic activity on oxidative stress. *Environ. Sci. Technol.* **2007**, *41*, 4158–4163.

[35] Bardhan, R.; Chen, W. X.; Perez-Torres, C.; Bartels, M.; Huschka, R. M.; Zhao, L. L.; Morosan, E.; Pautler, R. G.;

Joshi, A.; Halas, N. J. Nanoshells with targeted simultaneous enhancement of magnetic and optical imaging and photothermal therapeutic response. *Adv. Funct. Mater.* **2009**, *19*, 3901–3909.

[36] Kim, J.; Park, S.; Lee, J. E.; Jin, S. M.; Lee, J. H.; Lee, I. S.; Yang, I.; Kim, J.-S.; Kim, S. K.; Cho, M.-H. et al. Designed fabrication of multifunctional magnetic gold nanoshells and their application to magnetic resonance imaging and photothermal therapy. *Angew. Chem., Int. Ed.* **2006**, *45*, 7754–7758.

[37] Wang, L. Y.; Bai, J. W.; Li, Y. J.; Huang, Y. Multifunctional nanoparticles displaying magnetization and near-IR absorption. *Angew. Chem., Int. Ed.* **2008**, *47*, 2439–2442.

[38] Melancon, M. P.; Lu, W.; Zhong, M.; Zhou, M.; Liang, G.; Elliott, A. M.; Hazle, J. D.; Myers, J. N.; Li, C.; Stafford, R. J. Targeted multifunctional gold-based nanoshells for magnetic resonance-guided laser ablation of head and neck cancer. *Biomaterials* **2011**, *32*, 7600–7608.

[39] Ji, X.; Shao, R.; Elliott, A. M.; Stafford, R. J.; Esparza-Coss, E.; Bankson, J. A.; Liang, G.; Luo, Z.-P.; Park, K.; Markert, J. T. et al. Bifunctional gold nanoshells with a superparamagnetic iron oxide-silica core suitable for both MR imaging and photothermal therapy. *J. Phys. Chem. C* **2007**, *111*, 6245–6251.

[40] Tian, Q. W.; Hu, J. Q.; Zhu, Y. H.; Zou, R. J.; Chen, Z. G.; Yang, S. P.; Li, R. W.; Su, Q. Q.; Han, Y.; Liu, X. G. Sub-10 nm Fe_3O_4@$Cu_{2-x}S$ core–shell nanoparticles for dual-modal imaging and photothermal therapy. *J. Am. Chem. Soc.* **2013**, *135*, 8571–8577.

[41] Roch, A.; Muller, R. N.; Gillis, P. Theory of proton relaxation induced by superparamagnetic particles. *J. Chem. Phys.* **1999**, *110*, 5403–5411.

[42] Taboada, E.; Rodriguez, E.; Roig, A.; Oró, J.; Roch, A.; Muller, R. N. Relaxometric and magnetic characterization of ultrasmall iron oxide nanoparticles with high magnetization. Evaluation as potential T_1 magnetic resonance imaging contrast agents for molecular imaging. *Langmuir* **2007**, *23*, 4583–4588.

[43] Tromsdorf, U. I.; Bruns, O. T.; Salmen, S. C.; Beisiegel, U.; Weller, H. A highly effective, nontoxic T_1 MR contrast agent based on ultrasmall PEGylated iron oxide nanoparticles. *Nano Lett.* **2009**, *9*, 4434–4440.

[44] Hu, F. Q.; MacRenaris, K. W.; Waters, E. A.; Liang, T. Y.; Schultz-Sikma, E. A.; Eckermann, A. L.; Meade, T. J. Ultrasmall, water-soluble magnetite nanoparticles with high relaxivity for magnetic resonance imaging. *J. Phys. Chem. C* **2009**, *113*, 20855–20860.

[45] Shen, L.-H.; Bao, J.-F.; Wang, D.; Wang, Y.-X.; Chen, Z.-W.; Ren, L.; Zhou, X.; Ke, X.-B.; Chen, M.; Yang, A.-Q. One-step synthesis of monodisperse, water-soluble ultrasmall Fe_3O_4 nanoparticles for potential bio-application. *Nanoscale* **2013**, *5*, 2133–2141.

[46] Ye, X. C.; Zheng, C.; Chen, J.; Gao, Y. Z.; Murray, C. B. Using binary surfactant mixtures to simultaneously improve the dimensional tunability and monodispersity in the seeded growth of gold nanorods. *Nano Lett.* **2013**, *13*, 765–771.

[47] Frens, G. Controlled nucleation for the regulation of the particle size in monodisperse gold suspensions. *Nat. Phys. Sci.* **1973**, *241*, 20–22.

[48] Li, J.; Wu, J.; Zhang, X.; Liu, Y.; Zhou, D.; Sun, H. Z.; Zhang, H.; Yang, B. Controllable synthesis of stable urchin-like gold nanoparticles using hydroquinone to tune the reactivity of gold chloride. *J. Phys. Chem. C* **2011**, *115*, 3630–3637.

[49] Chen, L.; Ji, F.; Xu, Y.; He, L.; Mi, Y. F.; Bao, F.; Sun, B. Q.; Zhang, X. H.; Zhang, Q. High-yield seedless synthesis of triangular gold nanoplates through oxidative etching. *Nano Lett.* **2014**, *14*, 7201–7206.

[50] Lie, S. Q.; Wang, D. M.; Gao, M. X.; Huang, C. Z. Controllable copper deficiency in $Cu_{2-x}Se$ nanocrystals with tunable localized surface plasmon resonance and enhanced chemiluminescence. *Nanoscale* **2014**, *6*, 10289–10296.

[51] Xing, S. X.; Tan, L. H.; Yang, M. X.; Pan, M.; Lv, Y. B.; Tang, Q. H.; Yang, Y. H.; Chen, H. Y. Highly controlled core/shell structures: Tunable conductive polymer shells on gold nanoparticles and nanochains. *J. Mater. Chem.* **2009**, *19*, 3286–3291.

[52] Lin, M.; Guo, C. R.; Li, J.; Zhou, D.; Liu, K.; Zhang, X.; Xu, T. S.; Zhang, H.; Wang, L. P.; Yang, B. Polypyrrole-coated chainlike gold nanoparticle architectures with the 808 nm photothermal transduction efficiency up to 70%. *ACS Appl. Mater. Interfaces* **2014**, *6*, 5860–5868.

[53] Liu, Z. M.; Ye, B. G.; Jin, M.; Chen, H. L.; Zhong, H. Q.; Wang, X. P.; Guo, Z. Y. Dye-free near-infrared surface-enhanced Raman scattering nanoprobes for bioimaging and high-performance photothermal cancer therapy. *Nanoscale* **2015**, *7*, 6754–6761.

[54] Zha, Z. B.; Yue, X. L.; Ren, Q. S.; Dai, Z. F. Uniform polypyrrole nanoparticles with high photothermal conversion efficiency for photothermal ablation of cancer cells. *Adv. Mater.* **2013**, *25*, 777–782.

[55] Wang, Q.; Wang, J. D.; Lv, G.; Wang, F.; Zhou, X. K.; Hu, J. Q.; Wang, Q. G. Facile synthesis of hydrophilic polypyrrole nanoparticles for photothermal cancer therapy. *J. Mater. Sci.* **2014**, *49*, 3484–3490.

[56] Hong, J.-Y.; Yoon, H.; Jang, J. Kinetic study of the formation of polypyrrole nanoparticles in water-soluble polymer/metal cation systems: A light-scattering analysis. *Small* **2010**, *6*, 679–686.

[57] Feng, W.; Zhou, X. J.; Nie, W.; Chen, L.; Qiu, K. X.; Zhang, Y. Z.; He, C. L. Au/polypyrrole@Fe_3O_4 nanocomposites for MR/CT dual-modal imaging guided-photothermal therapy: An *in vitro* study. *ACS Appl. Mater. Interfaces* **2015**, *7*, 4354–4367.

[58] Tian, Q. W.; Wang, Q.; Yao, K. X.; Teng, B. Y.; Zhang, J. Z.; Yang, S. P.; Han, Y. Multifunctional polypyrrole@Fe_3O_4 nanoparticles for dual-modal imaging and *in vivo* photo-thermal cancer therapy. *Small* **2014**, *10*, 1063–1068.

[59] Vaitkuviene, A.; Kaseta, V.; Voronovic, J.; Ramanauskaite, G.; Biziuleviciene, G.; Ramanaviciene, A.; Ramanavicius, A. Evaluation of cytotoxicity of polypyrrole nanoparticles synthesized by oxidative polymerization. *J. Hazard. Mater.* **2013**, *250-251*, 167–174.

[60] Stewart, E. M.; Liu, X.; Clark, G. M.; Kapsa, R. M. I.; Wallace, G. G. Inhibition of smooth muscle cell adhesion and proliferation on heparin-doped polypyrrole. *Acta Biomater.* **2012**, *8*, 194–200.

[61] Ramanaviciene, A.; Kausaite, A.; Tautkus, S.; Ramanavicius, A. Biocompatibility of polypyrrole particles: An *in-vivo* study in mice. *J. Pharm. Pharmacol.* **2007**, *59*, 311–315.

[62] Peng, Y.-K.; Liu, C.-L.; Chen, H.-C.; Chou, S.-W.; Tseng, W.-H.; Tseng, Y.-J.; Kang, C.-C.; Hsiao, J.-K.; Chou, P.-T. Antiferromagnetic iron nanocolloids: A new generation *in vivo* T_1 MRI contrast agent. *J. Am. Chem. Soc.* **2013**, *135*, 18621–18628.

[63] Roper, D. K.; Ahn, W.; Hoepfner, M. Microscale heat transfer transduced by surface plasmon resonant gold nanoparticles. *J. Phys. Chem. C* **2007**, *111*, 3636–3641.

[64] Ding, X. G.; Liow, C. H.; Zhang, M. X.; Huang, R. J.; Li, C. Y.; Shen, H.; Liu, M. Y.; Zou, Y.; Gao, N.; Zhang, Z. J. et al. Surface plasmon resonance enhanced light absorption and photothermal therapy in the second near-infrared window. *J. Am. Chem. Soc.* **2014**, *136*, 15684–15693.